Study of lift enhancing mechanisms via comparison of two distinct flapping patterns in the dragonfly Sympetrum flaveolum

Y. H. Chen and M. Skote

Citation: Physics of Fluids (1994-present) **27**, 033604 (2015); doi: 10.1063/1.4916204
View online: http://dx.doi.org/10.1063/1.4916204
View Table of Contents: http://scitation.aip.org/content/aip/journal/pof2/27/3?ver=pdfcov
Published by the AIP Publishing

PHYSICS OF FLUIDS **27**, 033604 (2015)

Study of lift enhancing mechanisms via comparison of two distinct flapping patterns in the dragonfly *Sympetrum flaveolum*

Y. H. Chen and M. Skote[a)]
School of Mechanical and Aerospace Engineering, Nanyang Technological University, 50 Nanyang Avenue, Singapore 639798

(Received 19 December 2013; accepted 3 March 2015; published online 30 March 2015)

The computational fluid dynamic model of a live-sized dragonfly (*Sympetrum flaveolum*) hindwing is simulated according to the in-flight flapping motions measured in kinematic experiments. The flapping motion of the simulated wing is accomplished by dynamically re-gridding the wing-fluid mesh according to the established kinematic model for each flapping pattern. Comparisons between two distinct flapping patterns (double figure-eight and simple figure-eight) are studied via analysis of the aerodynamic forces and flow field structures. The result shows that additional lift is generated during supination and upstroke for the double figure-eight pattern, while maximum thrust is generated during pronation for the simple figure-eight pattern. In addition, through our comparisons of the different kinematics, we are able to reveal the mechanism behind the leading edge vortex stabilization prior to supination and the kinematic movement responsible for additional lift generation during supination. By increasing the translational deceleration during stroke-end rotations in the double figure-eight flapping pattern, a trailing edge vortex is formed which is stronger as compared to the single figure-eight flapping pattern, thus enhancing the lift. © *2015 AIP Publishing LLC.* [http://dx.doi.org/10.1063/1.4916204]

I. INTRODUCTION

Dragonflies are one of the most manoeuvrable flying insects, and capable of fast forward, hovering, and backward flights. In general, dragonflies operate each of their wings independently,[1,2] and the wing motion is readily controlled by the wing root muscles only,[3,4] making dragonfly an easier target for replicating its wing motions in man-made applications. Moreover, studies have shown that the flapping frequency of most flies is more than hundred hertz,[5,6] whereas the flapping frequency of dragonflies ranges from 36 Hz (Ref. 7) to 44 Hz.[8] The comparatively low flapping frequency reduces the noise upon approaching the prey. Dragonflies' high manoeuvrability, ready controllability, and low noise level make them suitable candidates for bionic Micro-air-vehicles (MAVs), which with the flight capabilities like dragonflies could be very useful in applications such as military reconnaissance, search and rescue, etc.

For a complete research, both fore- and hind-wings need to be studied. Maybury and Lehmann[9] studied the aerodynamic interaction between two robotic wings using the alignment of dragonfly wings. Their experimental results indicated hindwing lift modulation due to fore- and hind-wing interactions. In terms of the kinematics of the robotic wings, the wing trajectories were derived from a Fourier series, which is in accordance with our findings[10] and that of the others.[8,11] The stroke kinematics they used were adopted from an analytical model based on a single wing simulation,[12] and were applied to both fore- and hind-wings. Therefore, a generalized kinematic model of a single wing can be applied to both fore- and hind-wings in mechanical and computational modelling of

[a)]Author to whom correspondence should be addressed. Electronic mail: mskote@ntu.edu.sg. Tel.: (+65) 67904271. Fax: (+65) 67904062.

dragonfly wings. Since changes in hindwing motion have more effect on the aerodynamic properties than those of the forewing,[8] the present study focuses on the hindwing motion to encompass the various aerodynamic effects of the different flapping patterns. Furthermore, for applicability on MAVs, the single wing study presented here may very well be more preferable than a study on tandem wings.

In this paper, we carry out computational studies based on the in-flight flapping kinematics[10] of the dragonfly *Sympetrum flaveolum*. Two different flapping patterns were observed during the in-flight kinematic experiments: the simple figure-eight (S8) and the double figure-eight (D8) flapping pattern. The three-dimensional (3-D) movements of these two flapping patterns were expressed as kinematic models in a local body-fixed spherical coordinate system, and are incorporated into the wing motion of our computational fluid dynamic (CFD) simulations; hence, our CFD models of dragonfly flight closely mimic the live dragonfly flight.

From the past experimental and computational studies of insect flights, five of the most renowned unsteady aerodynamic mechanisms behind the lift enhancement in flapping wings are: (1) Weis-Fogh's "clap and fling" mechanism;[13] (2) delayed stall/leading edge vortex (LEV);[14] (3) added mass effect;[15–20] (4) Kramer effect/rotational lift;[21,22] and (5) wake capture.[23] Generally, Weis-Fogh's "clap and fling" mechanism is limited to insect wings with less restriction at the wing root so that the wings are able to touch each other at the dorsal most position, while the effect of added mass is most prominent at periods of acceleration and deceleration and is hence more pronounced during stroke reversals. Along with Kramer effect and wake capture, these four mechanisms deal with lift enhancement during the stroke reversals. On the other hand, the half strokes are covered by the delayed stall mechanism.

With our 3-D CFD modelling, we are able to specify which of the above-mentioned mechanisms are responsible for lift enhancement during dragonfly flapping. The augmented lift during wing rotations for D8 can however not be explained using the conventional theories. Through intense comparison of the two flapping patterns, we extract the subtle variations in the kinematics between S8 and D8 which cause a very different vortex dynamics and hence aerodynamic properties. In addition, we obtain a direct relationship between lift augmentation and wing kinematics, and hence are able to explain the lift enhancing properties due to the kinematic motion of the flapping wing. It is our hope that the present analysis of the CFD simulations will improve the understanding and appreciation of the relation between lift augmentation and changes in wing kinematics, as well as the designs of future biomimetic MAVs.

The remaining part of the paper is organized as follows. In Sec. II, the numerical methodology as well as the flapping wing kinematics is presented, followed by the verification of the numerical model in Sec. III. The results in the form of aerodynamic forces, streamline analysis, and pressure contours are presented in Sec. IV. In Sec. V, the conventional theories are utilized for explaining the lift enhancement. For the middle stage of the flapping cycle, where the wing changes from downward to upward motion (supination), the conventional theories are unable to account for the additional lift observed for D8, which leads to Sec. VI, where we present a new lift enhancing mechanism for the dragonfly during wing rotations through the comparative studies of the forces and vortex dynamics produced by the two different flapping patterns.

II. NUMERICAL METHODS

In this section, the CFD modelling of the dragonfly wing is presented with the geometry (A), computational domain and boundary conditions (B) of the virtual wing. In addition, the kinematics for the two different flapping patterns is introduced in Sec. II C. Finally, the dynamic re-meshing procedure incorporating the in-flight kinematic models of the two distinct flapping patterns is described (D), while the software specific details are given in (E).

A. Geometry of the virtual wing

In the present CFD modelling, the hindwing of the dragonfly is approximated by a rigid flat plate with a uniform thickness of 0.01 mm, which is 0.14% of the mean chord length. The planform

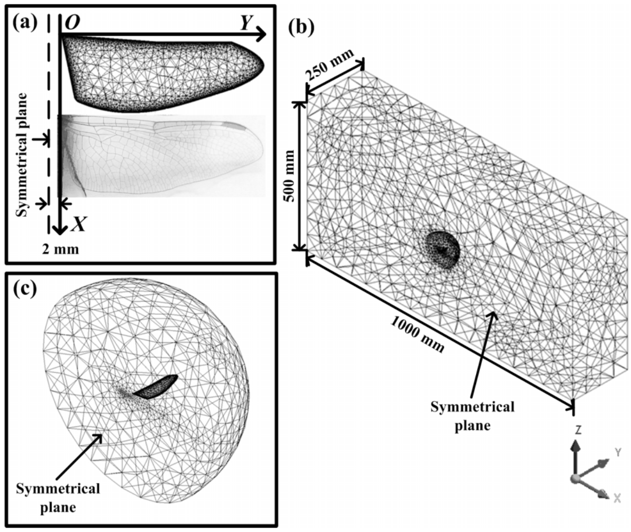

FIG. 1. Geometry and computational domain of the virtual dragonfly hindwing. (a) Top view showing the planform of the modelled hindwing and its real counterpart. The symmetrical plane lies at the midline of the insect thorax, which has a 2-mm distance from the wing root. (b) Overall computational domains, including a far-field and a near-field fluid domain. (c) The near field semi-spherical fluid domain.

of the model wing is traced from the hindwing of the dragonfly *Sympetrum flaveolum*, which is the same species used in obtaining the flapping kinematics. A top view showing the planform of the virtual and real wing is illustrated in Fig. 1(a). Both the real and virtual hindwing have a mean chord length of 7.11 mm and a planform area of 177.85 mm^2, with an aspect ratio of 7.03.

B. Computational domain and boundary conditions

The present CFD model, including the virtual dragonfly hindwing and the computational domain, was produced in ANSYS Workbench 2.0. The wing geometry and fluid enclosure were created by the Design Modeller in ANSYS Workbench, and were then meshed using tetrahedral elements to give a total of 1.16×10^6 volume cells around the wing. The real wing (for more details and material properties)[24] and the computational model with the numerical mesh are shown in Fig. 1(a). The overall computational domain shown in Fig. 1(b) was based on the symmetrical half of the physical domain of a wind tunnel with 0.5 m $\times$ 0.5 m $\times$ 1 m dimension. Only one flapping hindwing and the flow on the right of the plane of symmetry were computed. The effect of left hindwing was taken into account through the central mirroring condition. The overall computational domain consisted of a near- and a far-field fluid domain.

The near-field semi-spherical fluid domain shown in Fig. 1(c) was meshed such that the grid was denser near the tips and edges of the wing, and coarser towards the far-field. Hence, the viscous flow at the leading edge, trailing edge, and wing tip was captured with higher resolution. Since the wings of most insects travel approximately five chord lengths during an up- or down-stroke,[13] the near-field domain extended to a distance of six times the maximum chord length away from the wing root to avoid the unstable reflection of the solution at the near-field boundary.

The grids on the outer far-field domain carried the solution to the far-field boundary. The grids were mapped between the near-field and the far-field boundary faces and increased with a growth rate of 1.5, so that the grid points were clustered around the wing, and gradually increased in size towards the far-field.

Boundary conditions were applied at the far-field boundaries: at the inlet boundary, the velocity components were set to the free stream conditions with X-velocity of 1.7 m/s and 0 m/s in the other directions; at the outlet boundary, pressure was specified as the free-stream static pressure. Moreover, impermeable and no-slip wall conditions were applied to the interface of the wing and fluid. On the plane of symmetry, flow symmetry conditions were applied. As illustrated in Fig. 1(a), the plan of symmetry was not at the wing root, but at the midline of the insect thorax with a 2-mm distance from the wing root.

C. Kinematics of the modelled wing

Kinematic modelling of the locomotion of the dragonfly flapping flight was established by analysing the trajectory data collected during the in-flight experiments.[10] In dragonflies, the muscles controlling wing motions are restricted at the wing root. Thus, it is reasonable to dissect the wing motions into rotational movements about the pivoting wing root. Since the wing was modelled as a rigid flat plate, its orientation can be determined from the leading edge position of the nodus N, together with the wing attitude in the form of the angle of attack α. The position of N is described by the position angle ϕ_N and elevation angle θ_N. See Fig. 2 for the definitions.

In the local body-fixed spherical coordinate system shown in Fig. 2(a), the wing position was described by rotating the wing about the Z-axis with the position angle ϕ_N and rotating about the X-axis with the elevation angle θ_N. The wing attitude at a given position was determined from rotating the wing about the Y-axis by the geometric angle of attack α. As shown by the inserts (i) and (ii) in Fig. 2(a), the position angle ϕ is the acute angle between the positive Y-axis and the projected line of the leading edge on the X-Y plane; it is positive along the negative X-axis, and negative along the positive X-axis. And the elevation angle θ is the acute angle between the positive Y-axis and the projected leading edge on the Y-Z plane; it is positive above X-Y plane and negative below X-Y plane. α is the geometric angle of attack, determined at 60% wing length with respect to the free-stream velocity in X-direction. It is positive when the leading edge is above the trailing edge and negative when the trailing edge is above the leading edge. In this way, the position and attitude of a flapping dragonfly hindwing at any time instance were represented in the current kinematic model.

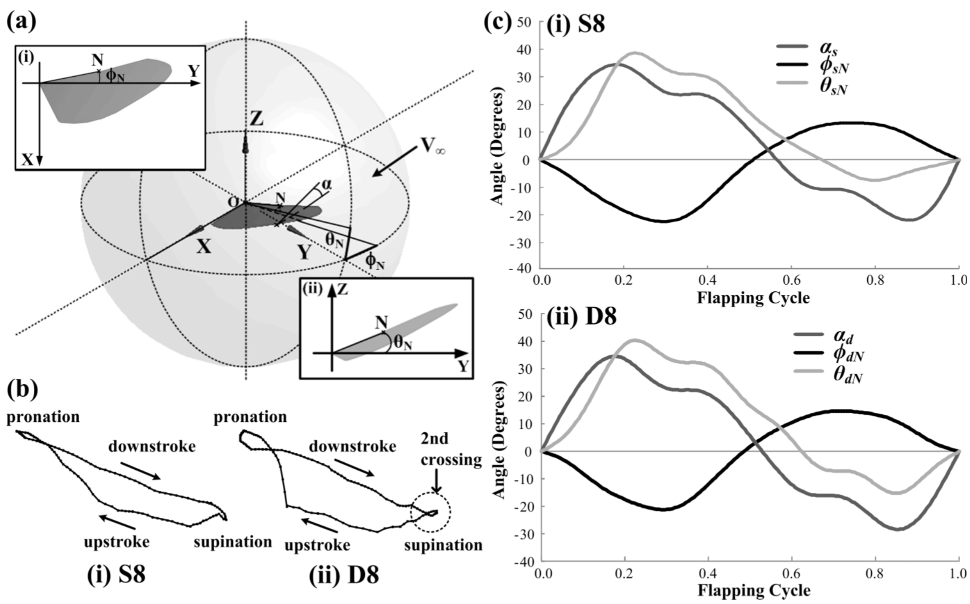

FIG. 2. Kinematic modelling. (a) Local body-fixed spherical coordinate system (ϕ, θ). α is the geometric angle of attack at 60% wing length with respect to the free-stream velocity in the X-direction. (i) The position angle ϕ is the acute angle between the positive Y-axis and the projection of the leading edge on the X-Y plane. ϕ is positive along the negative X-axis, and negative along the positive X-axis. (ii) The elevation angle θ is the acute angle between the positive Y-axis and the projection of the leading edge on the Y-Z plane. θ is positive above X-Y plane, and negative below it. (b) Projected trajectories of (i) simple figure-eight and (ii) double figure-eight flapping patterns on the X-Z plane in one complete flapping cycle consisting of four phases: downstroke, supination, upstroke, and pronation. (c) Time series of the position angle, the elevation angle, and the angles of attack of the hindwing during one complete flapping cycle. (i) Simple figure-eight flapping trajectory presented in ϕ_{sN}, θ_{sN}, and α_s. (ii) Double figure-eight flapping trajectory presented in ϕ_{dN}, θ_{dN}, and α_d. The curves are the fitted results from the Fourier series analysis of the in-flight kinematic data.[10]

From the kinematic analysis of dragonfly hindwing,[10] two distinct flapping patterns were detected: S8 and D8 figure-eight, as shown in Fig. 2(b). The trajectories represent the projected positions of the tracking points onto the X-Z plane as if viewed from the side of the dragonfly wing. The characteristic feature distinguishing the two different trajectories is the cross-over of the flapping path at stroke reversals. There is only one cross-over for the S8 flapping pattern, hence, the flapping path resembles a figure-eight (thus the naming); and there are two cross-overs for the D8 flapping pattern. In Fig. 2(b), one complete flapping cycle is sketched with the four phases of downstroke, supination, pronation, and upstroke indicated. Conventionally, the two half strokes (upstroke and downstroke) refer to the ventral-to-dorsal and dorsal-to-ventral motion of the wing, respectively; while the terms (supinates and pronates) are used to describe the stroke reversals where rapid changes of the angle of attack occur at the end of the half strokes.

For each flapping pattern, there is one kinematic model expressed in terms of ϕ_N, θ_N, and α, as shown in Fig. 2(c). Part (i) and (ii) in Fig. 2(c) illustrate the fitted curves of the position angle, the elevation angle, and the angle of attack through Fourier series analysis in one complete S8 and D8 flapping cycle, respectively. The flapping cycle is measured in a non-dimensional time ($\hat{t}$) ranging from zero to unity, so that a flapping cycle starts with the wing lying horizontally and levelling with the insect body (at $\phi = 0$, $\theta = 0$, and $\alpha = 0$), and ends when the wing moved back to that horizontal position. The full formulation of the kinematic modelling expressed in Fourier series can be found in Appendix B.

In addition, the reference length L_{ref} was equal to the mean chord length of 7.11 mm. The reference velocity U_{ref} was taken to be $2\Phi\omega R$, where Φ was the flapping amplitude in radians, ω the flapping frequency, and R the wing length. The Reynolds number Re can be calculated by

$$Re = \frac{U_{ref} L_{ref}}{\nu}, \tag{1}$$

where ν is the kinematic viscosity of air, 1.5×10^{-5} m^2/s. The flapping amplitude and frequency were 1.18 rad, 39.47 Hz and 1.17 rad, 38.46 Hz, for S8 and D8, respectively. With a wing length of 25 mm, Re was approximately between 1000 and 1100, similar to the typical Re value ($\sim 10^3$) in dragonfly flights.[25,26]

And, the advance ratio J is defined as

$$J = \frac{V_\infty}{U_{ref}}, \tag{2}$$

where V_∞ is the free stream velocity of 1.7 m/s. The advance ratio used in the present study is estimated as 0.75.

D. Dynamic re-meshing process

From the kinematic analysis of the dragonfly wings, the 3-D motion of the flapping wing was simulated with a three-step transformation of the rigid wing grids. The step-by-step dynamic re-meshing was proceeded in a positioning-elevating-feathering order. The wing root was defined as the pivot for the following rotational transformations of the wing grids in the local body-fixed coordinate system. First, the initial grids (at $\phi = 0$, $\theta = 0$, and $\alpha = 0$) were updated to the new positioned grids by rotating with the relative position angle ϕ' about the Z-axis. Second, the positioned grids were then rotated about the X-axis according to the relative elevation angle θ'. Finally, the positioned-and-elevated grids were updated according to the rotation of the relative angles of attack α' about the Y-axis. The relative angles are the difference in radians between the angles at the current time step and their counterparts at a previous time step. Thus, the wing grids are re-meshed and updated through the above mentioned rotational transformations at each instant.

E. Numerical technique

In the present simulation, the unsteady incompressible Navier-Stokes equations were solved using the commercial software ANSYS FLUENT. Since the characteristic Re of the dragonfly was less than 10^3, the flow was assumed laminar. By using the dynamic mesh feature in FLUENT, the

3-D motion of the hindwing was incorporated into the solver via a user-defined-function (UDF). The UDF defined the movement of the boundary layer mesh around the virtual wing, so that the overall mesh was deformed according to the kinematics of the flapping wing at each time step. Two sets of UDFs were used in order to replicate the two different flapping trajectories in dragonfly flight.

For the solution methods, the pressure-velocity coupling was accomplished via the SIMPLE algorithm. Moreover, the second-order upwind spatial discretization and the first-order implicit temporal discretization were used. For the convergence criteria, the residuals of continuity and velocities had to be reduced more than three orders of magnitude in each time step.

III. VERIFICATION AND VALIDATION OF THE COMPUTATIONAL MODEL

A series of verification and validation tests were conducted for the present computational model. First, the self-consistency of the numerical solver was verified in various levels of grid and time step refinements. After that, the simulations of the dragonfly flight were validated with the experimental and computational results of other researchers.

A. Self-consistency of the numerical solver

The verification of the numerical solver focused on its self-consistency in terms of the effects of time step size and grid refinement. Two different levels of time step size and grid refinement were used and combined into three distinct cases. The kinematic data of the D8 flapping pattern (as in Fig. 2(c)(ii)) are used when running the verification.

The baseline case involved a grid number of 1.16×10^6 volume cells and a time step size of 2.5×10^{-5} s. The time step size was then halved to form a second case of 1.16×10^6 volume cells and 1.25×10^{-5} s. The third case refined the grids to a total of 2.41×10^6 volume cells by halving the minimum size of the volume cell. The resultant vertical force and thrust coefficients (for definitions, see Sec. IV A) of the three cases shown in Fig. 3 demonstrate that the time step size and the grid refinement did not significantly affect the simulation results. Therefore, the baseline case setting of the time step and grid size was adopted in the present simulation of the dragonfly flight.

B. Validation of the numerical simulation

As a further demonstration of the feasibility of the present computational model, a validation test was established following the experimental set-up of Sane and Dickinson[27] in terms of kinematic motion. The computed lift and drag were then compared with the experimental results, as well as the computational results of Sun and Lan[28] for the same kinematic set-up. As both the experiment

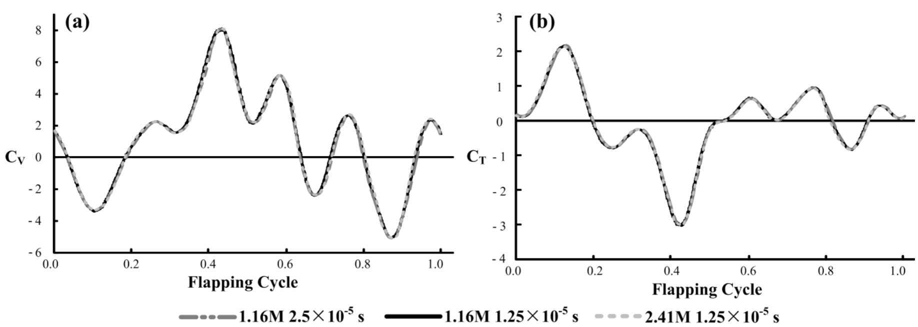

FIG. 3. Force coefficients versus flapping cycle for different grid and time step sizes. (a) Vertical force coefficient C_V and (b) thrust coefficient C_T with respect to non-dimensional time in one flapping cycle, for three different cases using the kinematics of the double figure-eight flapping pattern. The legends refer to 1.16×10^6 cells with a time step size of 2.5×10^{-5} s (1.16M 2.5×10^{-5} s), 1.16×10^6 cells with a time step size of 1.25×10^{-5} s (1.16M 1.25×10^{-5} s), and 2.41×10^6 cells with a time step size of 1.25×10^{-5} s (2.41M 1.25×10^{-5} s).

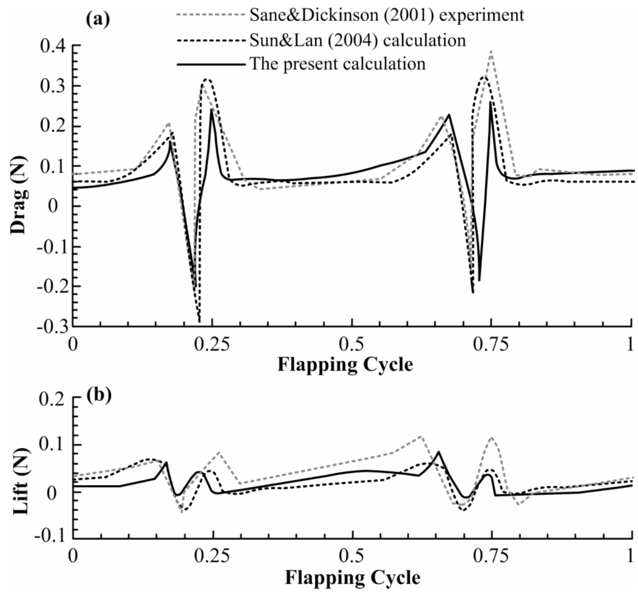

FIG. 4. Comparison of our computed lift and drag with the experimental results of Sane and Dickinson[27] and the computational results of Sun and Lan[28] in one corresponding flapping cycle.

and computation used for comparison are hovering flights, the advance ratio J was set to zero in our validation to simulate hovering flight. The comparisons are shown in Fig. 4.

The trends of the forces are very similar over the flapping cycle, with some variation in the amplitudes. Those slight differences are possibly due to the variations in the modelled wings in terms of thickness and wing shape. The aspect ratio of Sane and Dickinson's model wing is 7.49, which is similar but slightly higher than our aspect ratio of 7.03. The numerical results of Sun and Lan[28] also deviate from the experimental results of Sane and Dickinson[27] for the same set-up, but both of the numerical results in Fig. 4 are definitely within any reasonable error margin. In general, the agreement between ours and the others' computational and experimental aerodynamic forces is good. We are confident that the present CFD method can capture the unsteady aerodynamic forces and flows of the modelled dragonfly wings with reasonable accuracy.

In addition, the dynamic re-meshing process was applied to accomplish the kinematic motion in our validation calculation. A different approach was used in Sun and Lan[28] to achieve flapping motions. A good agreement in the resultant forces with Sun and Lan's calculation[28] validates the reliability of the present re-meshing technique.

IV. RESULTS FROM THE CFD SIMULATIONS

In this section, the results from the numerical simulations are presented. First, the aerodynamic forces and the flow fields are presented and compared for the two flapping patterns in Secs. IV A and IV B, respectively. In addition, Sec. IV C is devoted to the pressure distribution on the wing as a result of the vortex dynamics.

A. Evaluation of aerodynamic forces

In the present simulation, the Navier-Stokes equations are solved by finite volume methods and the resultant velocity, force and pressure are summarised from their respective components at the discretized cell centroids. The lift (L) and drag (D) forces of a flapping wing are the perpendicular and parallel components of the aerodynamic force on the wing with respect to the direction of wing motion, respectively. Resolving the lift and drag into the Z and X directions in our local body-fixed coordinate system gives us the vertical force (V) and thrust (T) of the wing.

All the force coefficients are non-dimensionalized with respect to the reference velocity U_{ref} and the reference area A_{ref} which is the wing planform area, so that the vertical force coefficient C_V, the thrust coefficient C_T, and the pressure coefficient C_p are defined as

$$C_V = \frac{V}{0.5\rho {U_{ref}}^2 A_{ref}}, \tag{3}$$

$$C_T = \frac{T}{0.5\rho {U_{ref}}^2 A_{ref}}, \tag{4}$$

and

$$C_p = \frac{P}{0.5\rho {U_{ref}}^2}, \tag{5}$$

where V is vertical force, T is thrust, P is pressure, and ρ is the air density.

The wing starts flapping from a stationary position, and the calculation stops when periodicity is approximately reached for the force and flow field generated, which in this case is approximately two cycles after the calculation starts (refer to Appendix A for verification of periodicity). Fig. 5 shows the computed vertical force and thrust coefficients for the two flapping patterns in one complete flapping cycle.

The non-dimensional time $\hat{t}$ of the flapping cycle is identical to that used Sec. II, so that one flapping cycle starts with the wing at $\phi = 0$, $\theta = 0$, and $\alpha = 0$, where it is towards the end of the upstroke, and ends when the wing returns to that position. The force coefficients of the first half cycle are very similar for both the flapping patterns, whereas the differences mainly occur during the second half of the flapping cycle. This is consistent with the two flapping patterns shown in

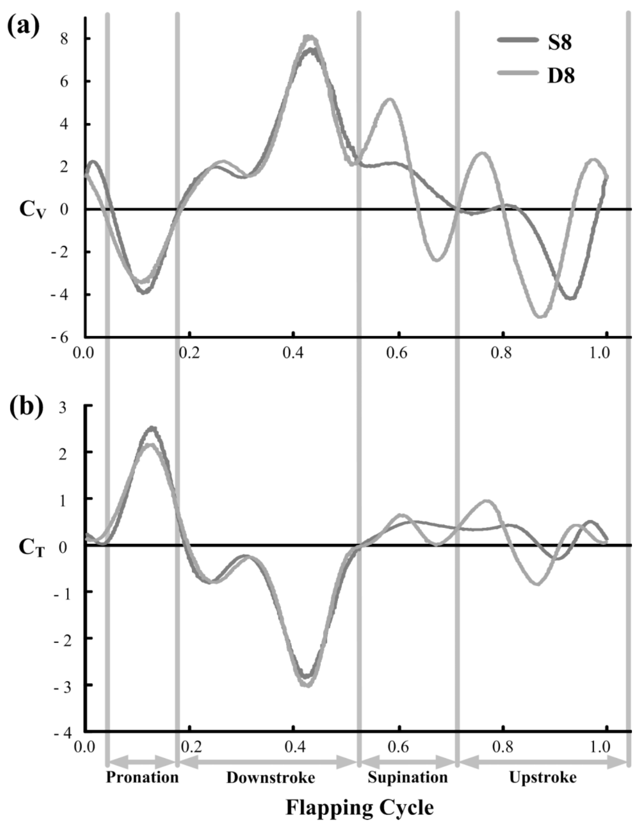

FIG. 5. Computed (a) vertical force coefficient C_V and (b) thrust coefficient C_T in one complete flapping cycle. One complete flapping cycle consisting of four phases: pronation, downstroke, supination, and upstroke.

Fig. 2(c), which differ mostly in the second half cycle, when the wing starts to supinate and move upstroke.

As illustrated in Fig. 5, most of the positive vertical force generates during downstroke for the both flapping patterns, which is consistent with other computational and experimental studies of flapping insects.[1,29–31] Nevertheless, additional lift is generated during supination and upstroke for D8.

Furthermore, the thrust is created during supination, upstroke, and pronation, with significant instantaneous thrust produced during pronation. Previous CFD simulations have suggested that thrust is created during upstroke and does not include supination and pronation.[25,31,32] The trajectories computed by Xu and co-workers[31] in hovering flights and by Wang and Sun[25] in forward flights are both simplified, so that the down- and upstroke motions are symmetrical to each other. In real forward flights, however, the duration of the two half strokes is different with longer downstroke.[8] Since the production of the aerodynamic forces depends on the timing of the stroke-end rotation and the stroke reversal,[22,33,34] a symmetrical stroke trajectory is inappropriate to use, and the conclusion that the thrust produced mainly in the upstroke of the dragonfly flight is not accurate.

In Fig. 5(a), there is only one large C_V peak at 71% of downstroke ($\hat{t}$ = 0.46) and no other comparable peaks in one complete cycle of S8. On the other hand, there are three more comparable C_V peaks when the wing is at 22% of supination ($\hat{t}$ = 0.60), and at 14% ($\hat{t}$ = 0.79) and 86% ($\hat{t}$ = 0.98) of upstroke in one cycle of D8. The trends of C_T are very similar for both the flapping patterns, as shown in Fig. 5(b). Both flapping patterns exhibit a single large C_T peak when the wing is also experiencing the maximum vertical force generation during pronation as indicated in Fig. 5(b).

A summary of the computed aerodynamic forces based on one hindwing is listed in Table I. The differences between the average vertical force and thrust coefficients in D8 and S8 are marginal. On the other hand, S8 provides a slightly larger maximum thrust. The maximum thrust of S8 boosts the dragonfly with a forward acceleration of 8.45 m/s.[2] The average weight of the dragonflies used in our experiments[10,24] is around 110 mg. The mean vertical force coefficient for a pair of hindwings in S8 and D8 gives an averaged force enough to support a weight of 127 mg and 131 mg, respectively, which is more than the force required to support the weight of the dragonfly for just the pair of hindwings alone. The computed mean thrust is positive, in accordance with the nature of forward flight. These results show the correct and reasonable trends in the forward flight of dragonflies, which further validate the robustness of the present computational model.

B. CFD-visualized streamlines during one flapping cycle

The LEV forming on a flapping wing determines to a large extent the generated lift. Streamlines are proved to be useful in identifying LEVs, though wake structure away from the wing cannot be detected, spanwise flows should be detected by streamlines alone.[35] In this section, computed instantaneous streamlines are presented for the same four phases of one complete flapping cycle as demonstrated in Fig. 5, in order to visualize the changes of LEVs due to the differences in the kinematic flapping patterns. Side views (projection on the Z-X plane) of the instantaneous streamlines around the wing are shown for each flapping pattern during each phase. Schematic drawings of the

TABLE I. Summary of the computed aerodynamic forces in one hindwing. $\bar{C}_V$ and $\bar{C}_T$ are the mean values of C_V and C_T, respectively. $C_{V,Max}$ and $C_{T,Max}$ are the maximum values of vertical force and thrust coefficients, respectively.

	S8	D8
$\bar{C}_V$	1.06	1.09
$\bar{C}_T$	0.025	0.087
$C_{V,Max}$	7.55	8.15
$C_{T,Max}$	2.95	2.47

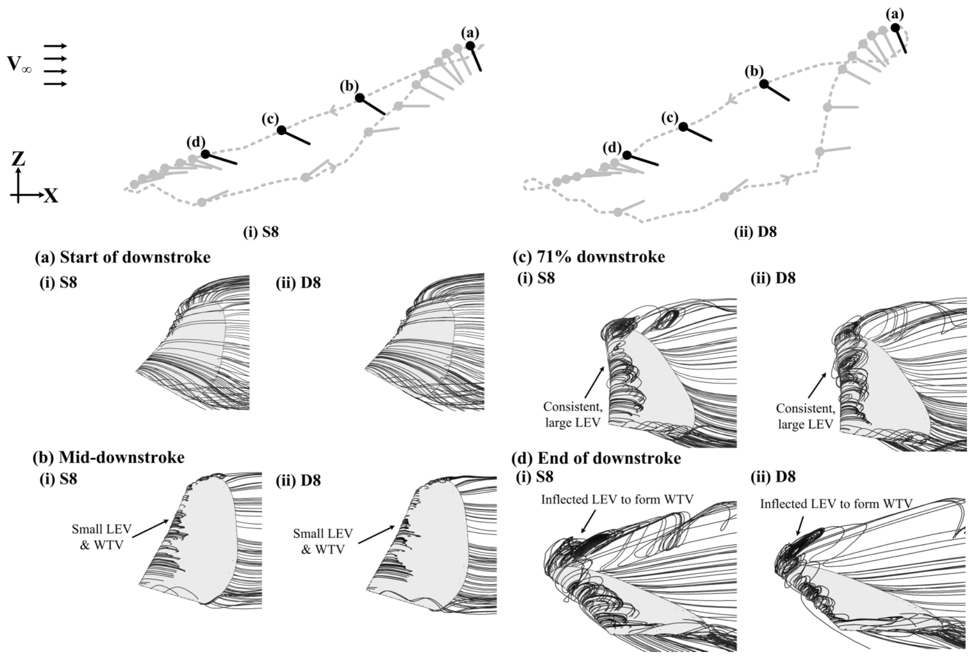

FIG. 6. Side view of the instantaneous streamlines of the hindwing (with corresponding schematic drawings of the wing position and attitude on top) during (a) start of downstroke ($\hat{t} = 0.19$), (b) mid-downstroke ($\hat{t} = 0.37$), (c) 71% downstroke ($\hat{t} = 0.46$), and (d) end of downstroke ($\hat{t} = 0.56$) for (i) S8 flapping pattern and (ii) D8 flapping pattern.

wing are displayed alongside the instantaneous streamlines, illustrating the position and attitude of the wing at each instant (Figs. 6–10). The wing chord is depicted by light grey solid lines showing wing attitude at 60% wing length with light grey solid dots marking the leading edge. The light grey dotted line indicates the wing-tip trajectory with the arrow showing the direction of wing motion. The highlighted black wings indicate the active wing positions at that particular phase, with each instant and flapping pattern labelled accordingly. Note that the wing attitude is not drawn to scale, but slightly exaggerated to clearly demonstrate the trend of change in the angle of attack during each phase. The remainder of this section is purely descriptive, while the analysis together with vorticity visualizations will be conducted later in Secs. V and VI.

1. During downstroke

The presence of LEV is clearly seen in Fig. 6 for both flapping patterns during downstroke. At the beginning of the downstroke, the flow is mostly attached, as shown in Fig. 6(a). Prior to mid-downstroke, the flow starts to separate at the leading edge and the LEV is formed. At this stage, the LEV is still small in diameter as seen from Fig. 6(b). As the wing proceeds further downstroke, the LEV grows in size and reaches its maximum near 71% of downstroke. As seen in Fig. 6(c), the LEV at 71% of downstroke is large and consistent with similar size and shape across the wing. As the wing moves towards the end of downstroke, Fig. 6(d) shows that the LEV does not shed off after maximum size reached at 71% of downstroke; instead, it inflects at the wing tip and continues with vortices trailing from the wing tip to form a wing tip vortex (WTV). The size and strength of LEV reduces as part of the LEV moves downstream with the WTV to form the starting vortex.

2. During supination

The difference between S8 and D8 becomes obvious during supination as seen in Fig. 7. At the beginning of supination, the flow structures are similar to those at the end of downstroke (see Figs. 7(a) and 6(d)). As the wing proceeds to 22% of supination, Fig. 7(b)(i) for S8 shows a LEV

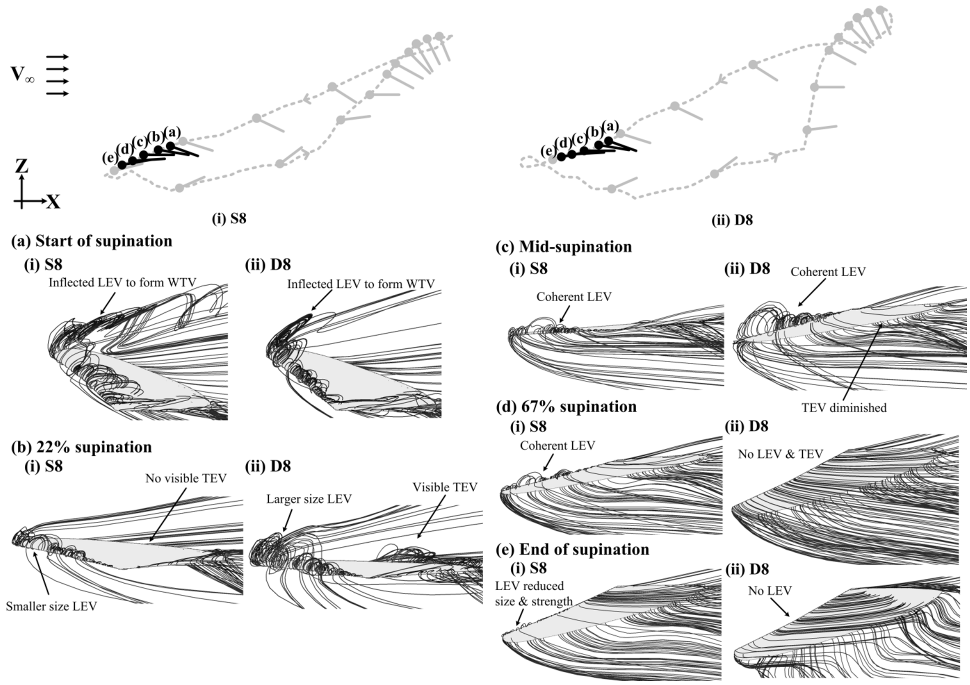

FIG. 7. Side view of the instantaneous streamlines of the hindwing (with corresponding schematic drawings of the wing position and attitude on top) during (a) start of supination ($\hat{t} = 0.56$), (b) 22% supination ($\hat{t} = 0.60$), (c) mid-supination ($\hat{t} = 0.65$), (d) 67% supination ($\hat{t} = 0.68$), and (e) end of supination ($\hat{t} = 0.74$) for (i) S8 flapping pattern and (ii) D8 flapping pattern.

of smaller size than that shown in Fig. 7(a)(i), with no visible trailing edge vortex (TEV). On the other hand, the presence of TEV is pronounced in D8 as seen in Fig. 7(b)(ii), as well as a larger size LEV as compared to its counterpart in S8. Thus, both the larger size of the LEV and the visible TEV correspond well to the larger vertical force for D8 shown in Fig. 5(a) at 22% of supination.

Towards the end of supination, the LEV decreases in size and strength as shown in Fig. 7(e). In the case of D8, the size of the LEV does not change much, whereas the TEV on the other hand diminishes from 22% to 50% of supination, as shown in (ii) of Figs. 7(b) and 7(c). As the wing proceeds to 67% of supination, both the LEV and TEV disappear, and the flow reattaches in D8. Compared to the small but consistent LEV in S8, the attached flows in D8 are adverse for additional lift generation during the second half of supination, which is reflected in Fig. 5(a) by the decreasing vertical force coefficients during the second half of supination.

3. During upstroke

At the beginning of upstroke, the flow in D8 is still attached whereas a small LEV is present on the dorsal side of the wing in S8. As the wing proceeds to 14% of upstroke, the situation reverses, as illustrated in Figs. 8(b)(i) and 8(b)(ii). At this time instant, no LEV is present for S8 whereas D8 exhibits a small but consistent LEV on the dorsal side of the wing, stretching from 60% of the wing length all the way to the wing tip. Referring to the schematic drawings in Fig. 8, the wing undergoes a gradual nose-down feathering from the start to 14% of upstroke, when the angle of attack increases from $-16°$ to $-28°$ as shown in Fig. 2(c). During this time, the low pressure caused by the LEV on the dorsal surface of the wing produces positive vertical force and thrust along the moderately nose-down feathering wing. Since the wing is tilting at a moderate negative angle of attack, and the LEV on the dorsal surface of the wing is either missing as in S8 or is minimal as in D8, the resultant thrust is positive but small in magnitude. On the other hand, the LEV which exists for D8 (although weak) is responsible for the higher lift in D8 as compared to S8.

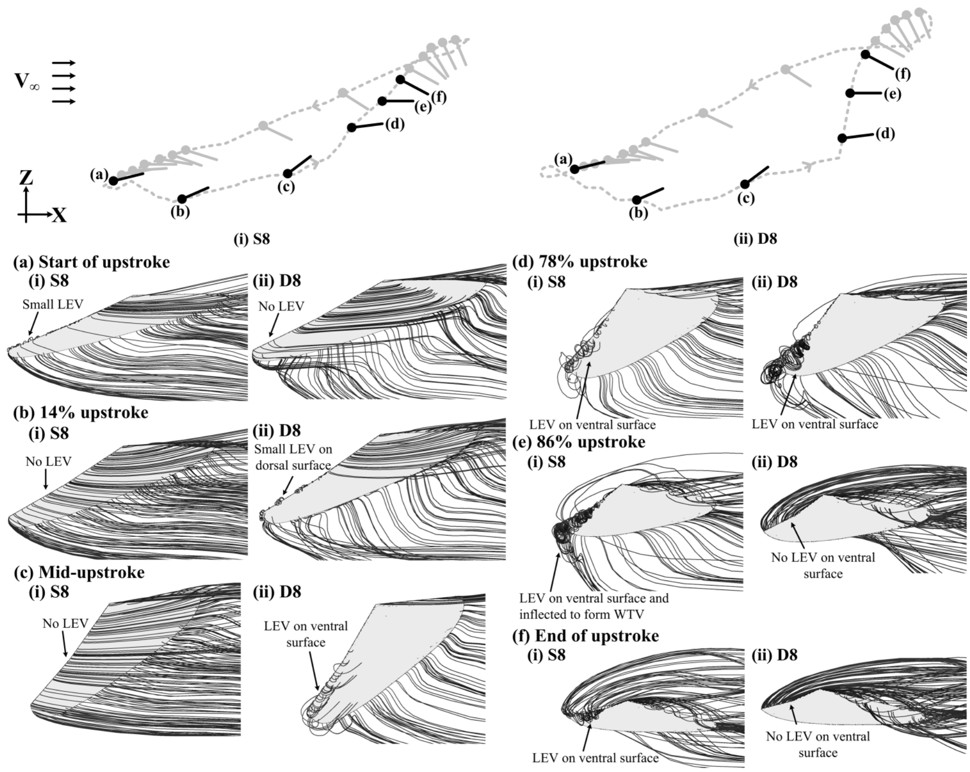

FIG. 8. Side view of the instantaneous streamlines and pressure contours of the hindwing (with corresponding schematic drawings of the wing position and attitude on top) during (a) start of upstroke ($\hat{t} = 0.74$), (b) 14% upstroke ($\hat{t} = 0.79$), (c) mid-upstroke ($\hat{t} = 0.90$), (d) 78% upstroke ($\hat{t} = 0.96$), (e) 86% upstroke ($\hat{t} = 0.98$), and (f) end of upstroke ($\hat{t} = 0.02$) for (i) S8 flapping pattern and (ii) D8 flapping pattern.

As the wing proceeds further to mid-upstroke, the small LEV in D8 shifts from the dorsal side of the wing to the ventral side and grows in size as shown in Fig. 8(c)(ii). The LEV on the ventral surface means that there is a low pressure zone under the near wing tip region. Thus, there is negative lift acting on the nose-down wing, which is confirmed by the negative vertical force and thrust coefficients at mid-upstroke shown in Figs. 5(a) and 5(b). Since no LEV on the ventral surface of the wing is present for S8, as shown in Fig. 8(c)(i), it is less detrimental for lift generation as compared to D8 at the same time instant. For S8, the LEV on the ventral surface of the wing occurs at 78% of upstroke, and remains attached to the ventral surface for the rest of upstroke and pronation.

As seen in Fig. 8(e)(i) for S8, the LEV on the ventral surface continues from 60% of the wing length to the wing tip, and inflects at the wing tip to form the WTV in the same manner as the LEV and WTV on the dorsal side of the wing. The WTV sheds quickly into the wake and leaves only the LEV on the ventral surface as shown in Fig. 8(f)(i). On the other hand, the LEV on the ventral surface is more intense and larger in size, indicating a stronger vortex in Fig. 8(d)(ii) for D8 than its just formed counterpart for S8 in Fig. 8(d)(i). From 86% of supination onwards, the flow in D8 becomes attached, the LEV has shed off the ventral surface of the wing and does not reappear until the latter half of pronation, as later shown in Fig. 9(b)(ii).

4. During pronation

During pronation, the wing flaps with a large angle of attack for both flapping patterns. As shown in Figs. 9(b)-9(d), the flow structures are very similar for both flapping patterns, namely, there is always a LEV on the ventral surface of the wing, with the exception of the absence of LEV at the start of pronation for D8 which is evident from Fig. 9(a).

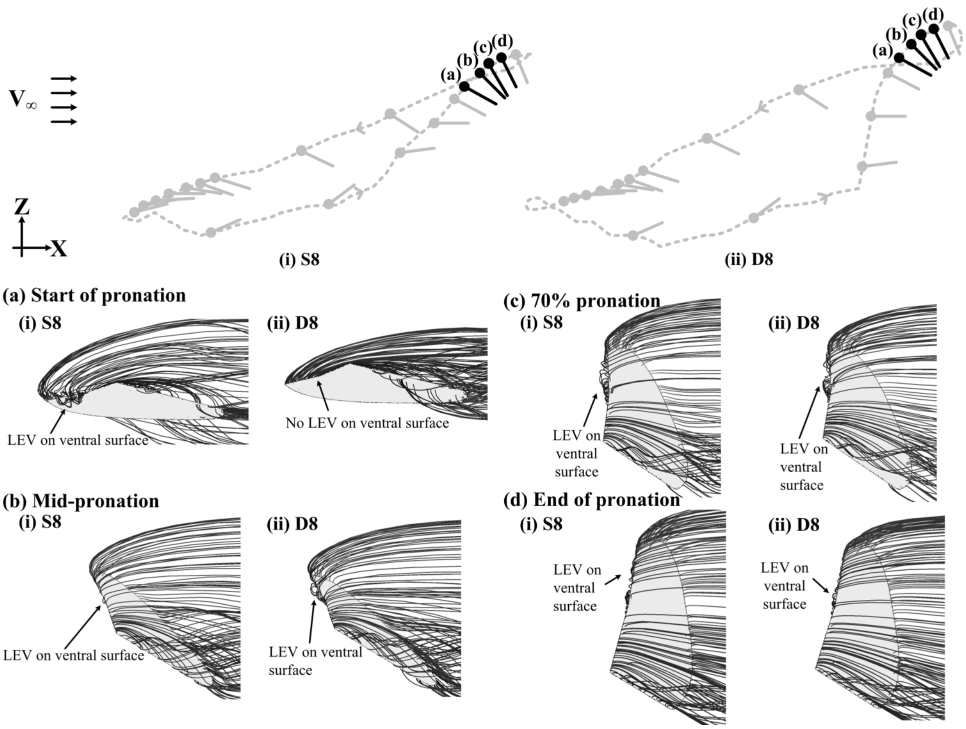

FIG. 9. Side view of the instantaneous streamlines of the hindwing (with corresponding schematic drawings of the wing position and attitude on top) during (a) start of pronation ($\hat{t} = 0.02$), (b) mid-pronation ($\hat{t} = 0.11$), (c) 70% pronation ($\hat{t} = 0.14$), and (d) end of pronation ($\hat{t} = 0.19$) for (i) S8 flapping pattern and (ii) D8 flapping pattern.

5. Summary

Overall, the complete flow sequence corresponds well with the aerodynamic coefficient history. For one complete flapping cycle, the distinction between the two flapping patterns appears during supination and upstroke. During the first half of supination, the presence of a larger coherent LEV and visible TEV enhances the lift generation in D8. As compared to D8, S8 shows coherent but smaller LEV and no visible TEV. This is in accordance with the force peak (shown in Fig. 5(a)) present for D8 but not for S8 during the first half of supination. Similarly, the force peak seen in Fig. 5(a) for D8 during first half of upstroke (14% of upstroke) is consistent with the small LEV present on the dorsal surface of the wing, whereas there is no LEV in S8.

C. Pressure coefficient contour

Figure 10 presents the top view of the pressure coefficient contour on the hindwing during each of the four phases corresponding to the extrema of C_V or C_T. At maximum C_V during downstroke, the corresponding pressure coefficient contours shown in column (i) of Fig. 10 indicate a low pressure zone on the dorsal side of the wing at the leading edge and across the wing span. The contours are similar for both flapping patterns and in accordance with the size and shape of the LEV acting on the wing as shown in Fig. 6(c). Column (ii) in Fig. 10 illustrates the pressure coefficient contour at 22% of supination, when a second maximum vertical force is produced in D8 but is absent in S8. The cyan-colour regions in Fig. 10(b)(ii) near the leading edge and trailing edge of the wing indicate the presence of the LEV and TEV for D8.

As described in Sec. IV B 3, at mid-upstroke, there is a low pressure zone under the near wing tip region in D8 but not in S8, thus the difference in pressure coefficient contour shown in column (iii) of Fig. 10. Since the wing is tilted at a moderate negative angle of attack at this instant, the relatively high pressure acting on the dorsal surface of the wing contributes to the relatively larger negative vertical force in D8 as compared to S8.

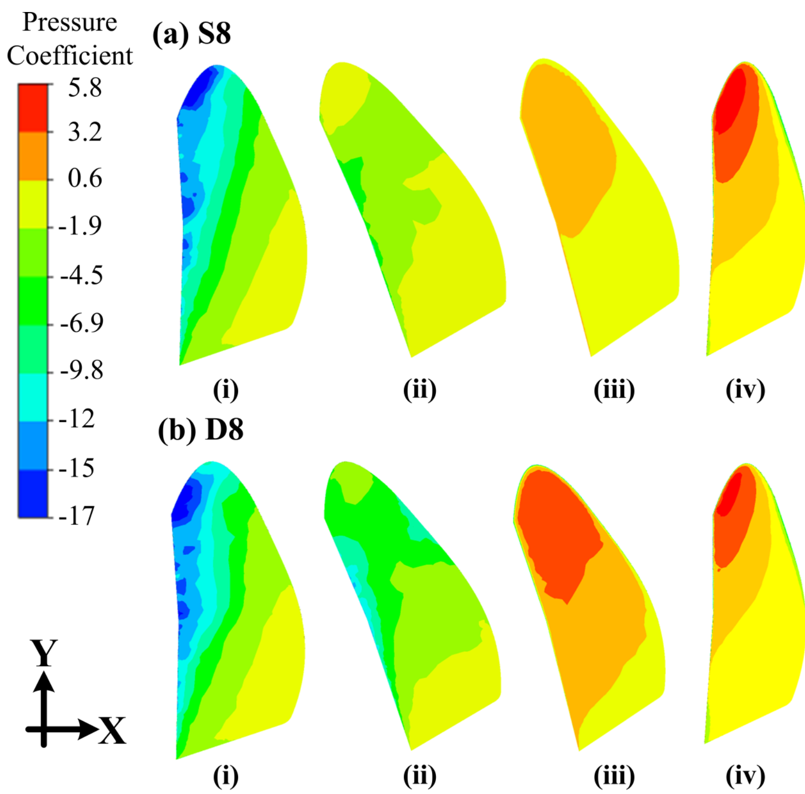

FIG. 10. Pressure coefficient contour at (i) maximum C_V at 71% of downstroke, (ii) 22% of supination, (iii) minimum C_V at mid-upstroke, and (iv) maximum C_T at 70% of pronation, for (a) S8 and (b) D8 flapping pattern, respectively.

As seen in column (iv) of Fig. 10, there is a high pressure zone on the dorsal surface of the wing, near the wing tip. Since the wing is inclined at a large positive angle of attack to the incoming flow stream at this point of time, the high pressure acting on the dorsal surface contributes largely to thrust. Therefore, high thrust is produced during pronation in accordance with the large peak shown in Fig. 5(b) during pronation.

V. UNSTEADY AERODYNAMICS OF DRAGONFLY FLIGHT

In this section, we will introduce the well-established mechanisms for lift generation. Using these, the lift enhancement during downstroke and upstroke are accounted for (Sec. V A). The following Sec. V B applies a well-known theory to explain the lift generation during pronation successfully. However, as will be shown, the existing theories cannot provide a satisfactory explanation for the lift peak during supination for the D8 flapping pattern; hence, the following Sec. VI will be devoted to this phenomenon.

The five most renowned unsteady aerodynamic models are (1) Weis-Fogh's "clap and fling" mechanism;[13] (2) delayed stall/LEV;[14] (3) added mass effect;[15–20] (4) Kramer effect/rotational lift,[21,22] and (5) wake capture.[23] In general, dragonflies are incapable of flapping their wings in a "clap and fling" fashion due to the restriction on their wing root muscles. Thus, we can rule out Weis-Fogh's "clap and fling" mechanism in dragonfly flight. However, which one of the other mechanisms is responsible for the lift augmentations or—if any other factor is in play—still remains controversial to researchers in this area.

As demonstrated by several researchers, the lift enhancing feature of LEV is due to delayed stall during the half strokes in both hovering and forward flights of small flapping insects.[14,23,28,29,36] Nagai and co-workers have shown through their experimental and numerical studies that delayed stall is the effective mechanism used during half strokes, also in flapping forward flights.[36] On the

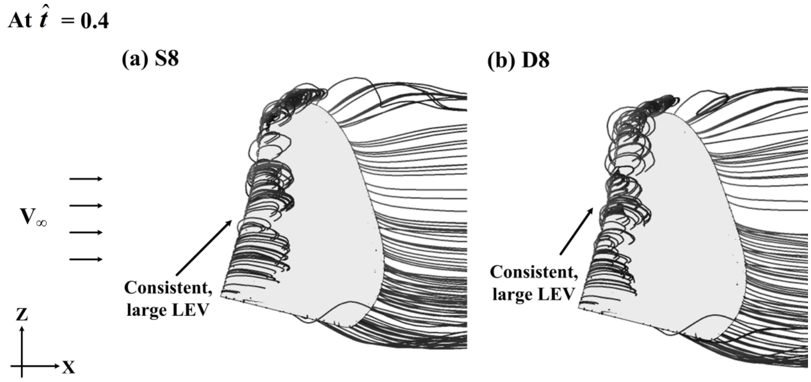

FIG. 11. Side view of the instantaneous streamlines of the hindwing at $\hat{t} = 0.40$ during downstroke for (a) S8 flapping pattern and (b) D8 flapping pattern.

other hand, the rotational lift mechanism,[22] the added mass effect,[15–20] and wake capture mechanism[23,37,38] are the most controversial mechanisms that might be responsible for lift augmentation during the stroke-end rotations of small insect flight. In the next two Secs. V A and V B, we will verify and discuss the mechanisms used during the half strokes and stroke-end rotations of dragonfly flight with our simulation results.

A. Verification of the lift enhancing mechanism during half strokes

The formation of LEV is claimed to be the cause of lift enhancement during each half stroke.[14,23,28,29,36] The maximum lift usually occurs during downstroke via a mechanism called delayed stall. A wing can travel at high angles of attack for a brief period prior to stall, to produce additional lift with the creation of a large LEV. Such mechanism is known as delayed stall.

In the present dragonfly simulation, the modelled wing is moving with the pre-set kinematics shown in Fig. 2(c). The angle of attack curve is almost constant from $\hat{t} = 0.30$ to $\hat{t} = 0.40$ in Fig. 2(c), which corresponds to the period that the large LEV is created and closely attached to the leading edge on the dorsal surface of the wing as demonstrated by the instantaneous streamlines at $\hat{t} = 0.40$ in Fig. 11. During this period, the wing maintains an angle of attack of 25°, which is comparable to the stall angle of attack (roughly 15°–25°) from a free-flying dragonfly in steady flow.[1] Hence, it is verified and confirmed via the present CFD simulation that delayed stall is the cause of maximum lift (accompanied by a large LEV) during downstroke of dragonfly flight, as concluded by Ellington and co-workers.[14]

Furthermore, as already discussed in Sec. IV B and illustrated in Fig. 8, the lift enhancements in D8 during upstroke are closely related to the formation of LEV as well. This relation can be summarized as follows: the dorsal LEV in D8 at 14% of upstroke (Fig. 8(b)) enhances the lift, while the ventral LEV in S8 at 86% of upstroke (Fig. 8(e)) creates negative lift. Similarly, as seen in Fig. 5(a), a large negative C_V peak exists for D8 at mid-upstroke which is related to a LEV on the ventral side of the wing (see Fig. 8(c)).

B. Verification of the lift enhancing mechanism during stroke-end rotations

Referring to Figs. 2 and 5, the wing kinematics and force generation are studied to verify the effect of rotational lift during stroke-end rotations. Note that an increase in the values of the angle of attack means a clockwise axial rotation, while a decrease in the value shows a counter-clockwise axial rotation. As seen in Fig. 2(c) and the schematic drawings in Fig. 9, the wing is rotating in a clockwise direction with a backward and upward translation during pronation. Thus, the rotation produces a counter-clockwise circulation in the fluid, which subtracts from the lift generated by the translating wing alone. This explains the sharp drop in vertical force during pronation as shown in Fig. 5(a).

However, the Kramer effect/rotational lift is unable to account for the vertical force peak which is present in the first half of supination for D8, but which is absent for S8. In both cases, the wing is rotating in the same counter-clockwise direction and translating in the forward and downward direction, as demonstrated in the schematic drawings in Fig. 7.

Furthermore, the contribution of added mass effects has been discussed by various researchers in the context of small insect flights.[16–20,39] The instantaneous force component due to the inertia of the added mass of the fluid can be derived from Sedov's[18] equations acting on a two-dimensional wing. By integrating Sedov's[18] equations along the wing span, we are able to estimate the force F_a due to added mass on a three-dimensional wing using the following formula:

$$F_a = 0.25\rho\pi R\bar{c}^2\Bigg[R(\ddot{\phi}\sin\alpha + \dot{\phi}\dot{\alpha}\cos\alpha - \ddot{\theta}\cos\alpha - \dot{\theta}\dot{\alpha}\sin\alpha) \times \int_0^1 \hat{c}^2(\hat{r})d\hat{r} - 0.5\bar{c}\ddot{\alpha}\int_0^1 \hat{c}^2(\hat{r})d\hat{r}\Bigg], \tag{6}$$

where ρ is the air density; R is the wing length; $\hat{r}$ is the non-dimensional axial position along the wing span, $\hat{r} = r/R$; $\bar{c}$ is the mean chord length; $\hat{c}(\hat{r})$ is the non-dimensional chord length,[15] $\hat{c} = c/\bar{c}$; ϕ and θ are the position angle and the elevation angle defined earlier in the wing kinematics (see Fig. 2) and α is the geometric angle of attack.

The resultant force F_a acts normal to the wing surface. In order to compare with our lift coefficients, F_a needs to be resolved into the vertical direction with respect to the free-stream flow. Hence,

$$F_{a,\mathrm{v}} = F_a\cos\alpha. \tag{7}$$

This force $F_{a,v}$ is then non-dimensionalized by the constant force $0.5\rho {U_{ref}}^2 S_{ref}$ as in the definition of lift and drag coefficients. Fig. 12 illustrates the time series of the force coefficients due to added mass effect and the corresponding vertical force coefficients for the two flapping patterns during supination. As seen in Fig. 12, the added mass effect is incapable to account for the vertical force generated during supination.

In addition, past smoke experiments[1] and single-wing simulations[12] of dragonfly flights have shown no interaction of the wake elements with the wing during stroke reversals. Wang[12] claimed that the figure-eight flapping patterns create a self-induced flow which sweeps away the vortices from the wing so that they do not interfere with the reversing wing. Quad-wing simulations have also suggested that the interaction of the hindwing with the shedding vortices from the forewing is not very strong and detrimental to the lift generation.[25,28] Fig. 13(b) illustrates the wing-wake interaction hypothesis proposed by Dickinson and co-workers.[21,37] In Fig. 13(c), the vorticity flow

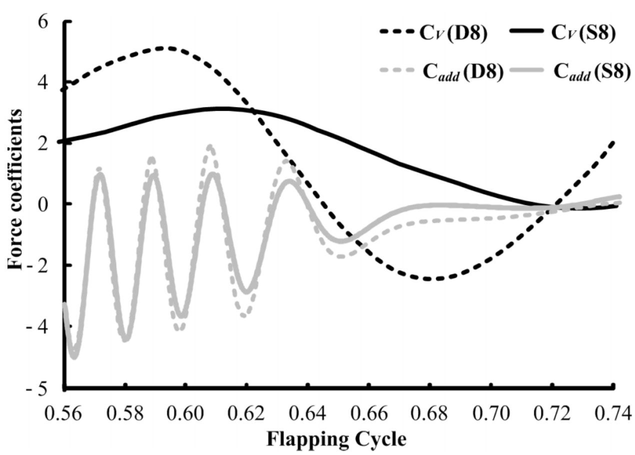

FIG. 12. Time series of the force coefficients due to added mass effect (C_{add}) and the corresponding vertical force coefficients (C_V) for the two flapping patterns (D8 and S8) during supination.

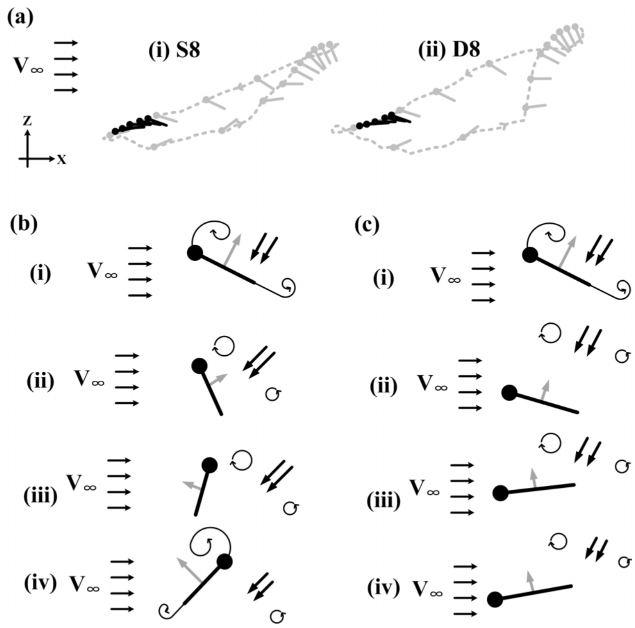

FIG. 13. Wing-wake interaction. The cross-section of the wing is depicted by black solid lines showing wing attitude at 60% wing length with black solid dots marking the leading edge. The black double arrows indicate the strong flow produced by the pair of counter-rotating vortices, and the grey arrow indicates the aerodynamic force generated on the wing. (a) Schematic drawing of our dragonfly wing position and attitude in one complete flapping cycle for (i) simple figure-eight and (ii) double figure-eight flapping pattern. The light grey dotted line indicates the wing-tip trajectory with the arrow showing the direction of wing motion. (b) The hypothesis of wing-wake interaction/wake capture proposed by Dickinson and co-workers.[21,37] (c) Schematic drawing (the positions of the vortices are deduced from the vorticity flow fields) of our dragonfly wings during supination showing why the hypothesis of wake capture is inapplicable to our dragonfly flight.

fields and the wing positions of our dragonfly wing are sketched in a similar way. It is shown in Fig. 13 that the hypothesis of wake capture is much depending on the wing position and attitude as well as the timing of the stroke-end rotation and the stroke reversal. From the schematic drawings of wing position and attitude in Fig. 13(a), it is illustrated clearly that the stroke-end rotations precede stroke reversals (rotation advanced) in our dragonfly forward flight. As shown in Fig. 13(c), once the vortices shed from the wing into the wake, they move in the opposite direction of the rotating and translating wing, and do not interact with the wing after stroke reversal. Therefore, wake capture is not applicable to our dragonfly flight, though it might be used by other insects.

Since the previous established mechanisms are unable to explain the additional vertical force generated in D8 during supination, we are motivated for a search of other mechanisms responsible for the vertical force peak during the supination. In the following Sec. VI, we will propose a new lift enhancing mechanism deduced from comparisons between the two distinct flapping patterns.

VI. PROPOSED LIFT ENHANCING MECHANISM DURING SUPINATION VIA VORTEX STABILIZATION

The two flapping patterns (S8 and D8) studied in the present simulation exhibit distinct trajectories although the trends in the angle of attack are similar. On the other hand, the lift enhancement shows great difference for the two distinct flapping patterns, especially during supination which is the focus of this section.

As seen from previous experimental and computational studies, the lift augmentation relies heavily on the size and stability of the LEV.[1,14,40] The longer the LEV remains closely attached to the flapping wing, the longer the insect enjoys high lift. Thus, the underlining mechanism of lift enhancement depends largely on the stabilization of the vortex, so that it remains attached to the wing for as long as possible.

Several papers have provided detailed reviews of the factors influencing the LEV generation and stability, such as the mode of hovering or forward flight,[25,28,41] the Reynolds number,[42] the aspect ratio or wing planform.[21,43,44] In general, *Re* does not change significantly with respect to the mode of hovering or forward flight.[25] In addition, experiments on free flying dragonflies have shown that there is little correlation between the flapping frequency, the angle of attack during half-strokes, and the stroke amplitude with the velocity and overall aerodynamic force generated during flight.[8] Wakeling and Ellington[8] also suggested that precise control of lift generation by the flapping wings may be achieved via small changes in the timing and kinematics of the wing rotations at stroke reversals.

In our search of other lift enhancing mechanisms during the supination, we thus focus on the mechanisms that are able to bind the vortex to the wing for a longer time through studies of how the changes in kinematic arrangements lead to the difference in vertical force generation, while keeping the other factors (flight mode, *Re*, and aspect ratio) identical in the two different flapping patterns.

It has been reported that the presence of axial flow depends on the Reynolds number of the flight regime[43] with the axial flow present at high *Re* (∼1400) and absent at low *Re* (∼120). However, axial flows have been reported in rotational wings at low *Re* (∼100).[45] Moreover, the axial flow is absent in both the present flow simulation and the visualisation experiments of Thomas and co-workers[1] in dragonfly flights with typical *Re* values ranging from 800 to 2000.[25,26] Other flow visualisation and CFD studies have also indicated that the axial flow is not necessary for stabilizing the vortex.[34,46]

Thomas and co-workers claimed that an increase in the angle of attack alone causes the formation, growth, and stabilization of the LEV during dragonfly flapping.[1] However, as our pre-set kinematics defines similar time series of the angle of attack for the two different flapping patterns, changes in the angle of attack are unlikely fully responsible for the formation, growth, and stabilization of the vortex. Nevertheless, the distinct flapping kinematics of the wing certainly plays a part in the lift enhancing mechanisms.

According to the kinematics of the flapping patterns shown in Fig. 2(c), the trends of the angle of attack and the position angle are very similar for the two flapping patterns during supination.

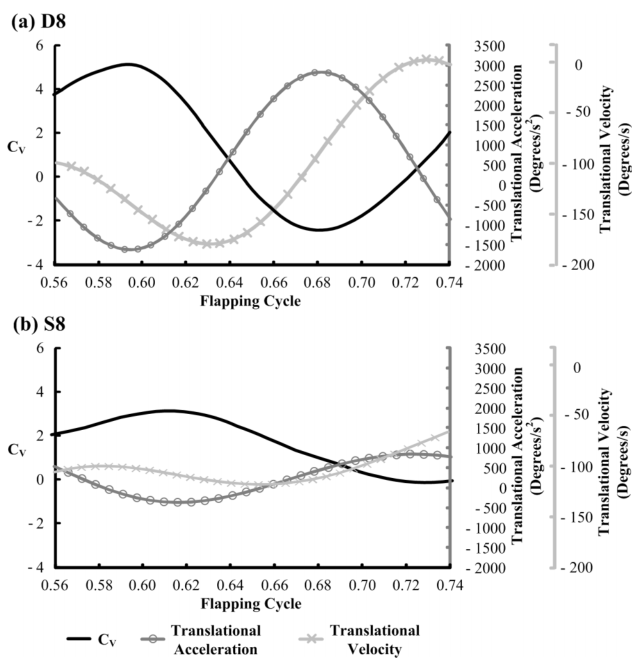

FIG. 14. Time series of the translational acceleration, the translational velocity and the corresponding vertical force coefficients for the two flapping patterns during supination.

The main difference is in the changes of the elevation angle, which is responsible for the different flapping trajectories.

In Fig. 14, the translational acceleration, the translational velocity and the corresponding vertical force coefficients are plotted for the two flapping patterns during supination. Note that though it is referred to as translation, it is in fact the elevational rotation of the wing about the wing root. Thus, the translational acceleration is expressed in degrees per second square and the translational velocity is expressed in degrees per second. As shown in Fig. 14, the minimum and maximum of the translational acceleration correspond to the maximum and minimum vertical force coefficient, respectively, for both D8 and S8 during supination. Fig. 14 also illustrates that as the translational acceleration decreases, the vertical force coefficient increases and vice versa. Thus, the transitional acceleration is directly correlated to the vertical force. As demonstrated in Fig. 12, it is clear that this correlation between the force increment and the translational acceleration is different from the added mass effect.

Comparing Figs. 14(a) and 14(b) reveals that the more pronounced change in the amplitude of the translational acceleration in D8 leads to a significant boost and drop of vertical force coefficients in D8 compared to the flatter curve in S8. According to Fig. 2(c), the wing undergoes a nose-down feathering while translating forward and downward in both D8 and S8 during supination. With reference to the wing motion, Fig. 14 can be interpreted as follows: (1) when the wing is moving downward and accelerating downward, C_V increases; (2) when the wing is moving downward but accelerating upward, C_V decreases.

From the above analysis, it is evident that increasing the translational acceleration in the same direction of the wing motion results in vertical force augmentation. In preparation of the second crossing (as shown in Fig. 2(b)) in D8, the wing moves further downward as compared to the S8 flapping pattern. The larger downward acceleration of the elevation angle at the beginning of supination in D8 leads to the additional lift generation in D8.

By investigating the vortex dynamics, the mechanism behind the above described lift enhancement can be explained. As will be demonstrated in the following, the larger translational acceleration for D8 produces a more significant TEV which generates lift peak during supination. As shown by the streamlines in Fig. 6, a clear distinction between S8 and D8 is that no TEV is visible for the latter. To verify the structure of the vortex system, vorticity plots are presented in Fig. 15.

In Fig. 15, the vorticity contours, velocity vectors, and pressure coefficients are plotted as projections on a vertical plane at 75% wing length for several time instants from near the end of downstroke to mid-supination, for both flapping patterns. The flows around the wings indicated by the velocity vectors are sketched with red arrows for better illustration. The wing chord at 75% wing length is marked with a black solid line. The wings in Fig. 15 are viewed from identical perspective as in Figs. 6 and 7, except in Fig. 15(f), where the view has been rotated for clarity.

In Fig. 15(a), the large area of negative pressure on the dorsal surface of the wing is caused by the large LEV attached on the wing at the time ($\hat{t} = 0.48$) after the maximum vertical force is achieved at 71% of downstroke ($\hat{t} = 0.46$) for both flapping patterns. Comparing all corresponding vorticity, velocity vectors, and pressure coefficients plots in Figs. 15(a)–15(c), all trends indicate that the LEV reduces in strength but remains attached on the dorsal surface of the wing after it reaches maximum size and strength at 71% of downstroke ($\hat{t} = 0.46$) until the start of supination ($\hat{t} = 0.56$), in both flapping patterns.

Figs. 15(b) and 15(c) show the vortex dynamics just before the end of downstroke and just after the start of supination, respectively. From Figs. 15(b) to 15(c), the vorticity contours show that the LEV reduces in size and strength but does not detach from the wing, and the vorticity contours partly move downstream as the wing starts nose-down feathering during supination in Fig. 15(c); while the pressure contours indicate a low pressure zone moving downstream from Figs. 15(b) to 15(c).

At the end of downstroke and the start of supination, the instantaneous streamlines in Figs. 6(d) and 7(a) show that the LEV inflects at the wing tip to form a WTV which curves around the wing tip towards the trailing edge. Thus, when the wing starts the swift nose-down feathering and downward translation at the beginning of supination, the WTV which carried part of the LEV sweeps upward and backward. In Fig. 15, the vortex dynamics plots are taken at the vertical plane at 75% wing

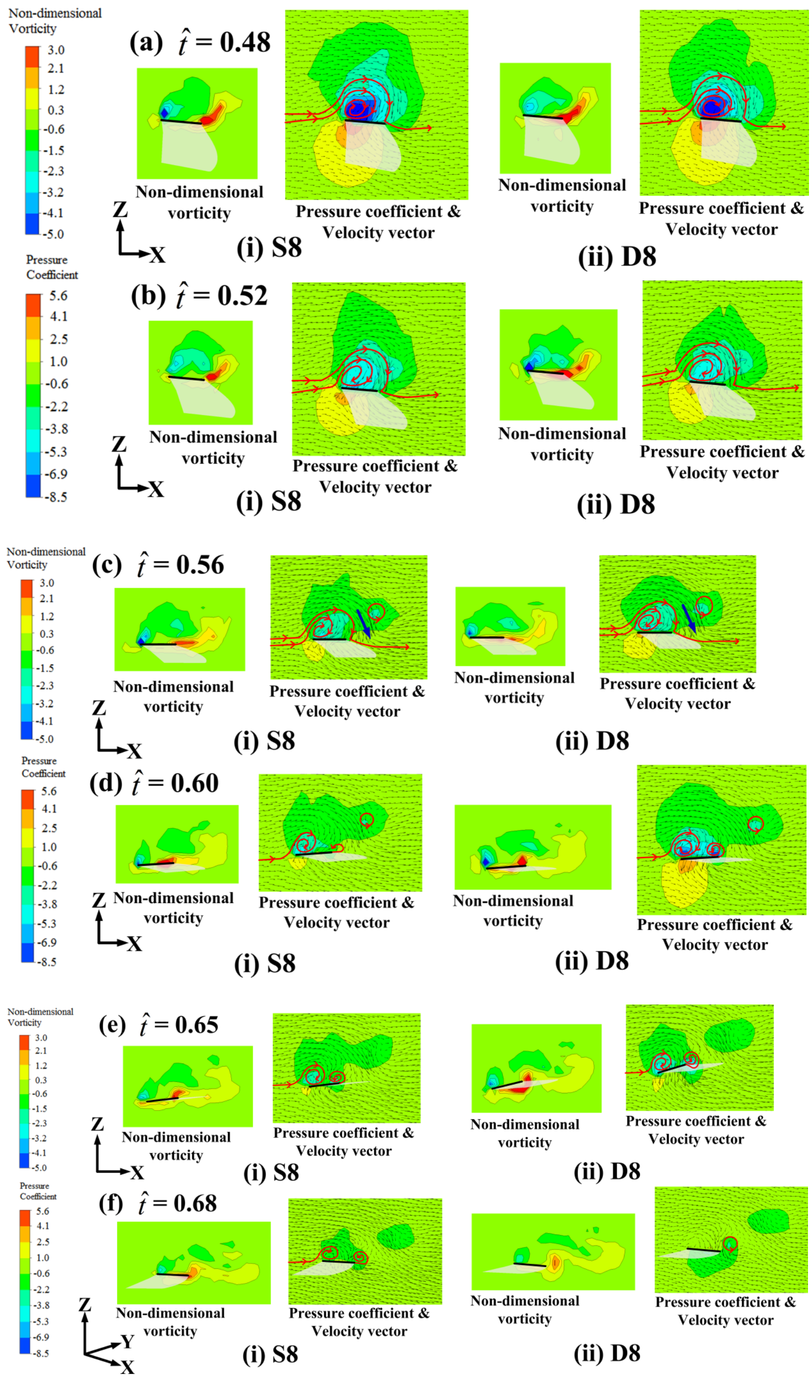

FIG. 15. Time history of vortex dynamics before and during supination at (a) right after 71% of downstroke ($\hat{t} = 0.48$), (b) right before end of downstroke ($\hat{t} = 0.52$), (c) right after start of supination ($\hat{t} = 0.52$), (d) 22% of supination when C_V reaches maximum value during supination ($\hat{t} = 0.60$), (e) mid-supination ($\hat{t} = 0.65$), and (f) 67% of supination when C_V drops to minimum value during supination, for (i) S8 flapping pattern and (ii) D8 flapping pattern. Contours of the spanwise vorticity components are plotted as projections on the vertical plane at 75% wing length (left), whereas superimposed plots of velocity vectors and pressure coefficients are shown at 75% wing length (right), for each time instant and flapping pattern.

length, which cuts through the curving WTV that has moved downstream. This curving WTV is clearly indicated by an additional low pressure zone in Fig. 15(c).

Moreover, the velocity vector plots in Fig. 15(c) show a backward and downward jet (highlighted with a blue arrow) produced in the intervening region of the two low pressure zones, which in turn produces an upward and forward force. This explains the bounce back of vertical force and positive thrust at the beginning of supination, as demonstrated in Figs. 5(a) and 5(b).

As the wing proceeds further during supination, the LEV is strengthened by the presence of a TEV as indicated by the more intensive positive vorticity contour and the negative pressure contour at both the leading and trailing edge of the wing in Figs. 15(d) and 15(e) for both S8 and D8, with D8 having more prominent vorticity contours at the leading and trailing edges. Meanwhile, the WTV moves further downstream and finally sheds in the wake as shown by the detached negative vorticity moving downstream and the negative pressure zone in the wake in Figs. 15(d)–15(f).

In Figs. 15(a)–15(c), the positive vorticity shown at the trailing edge of the wing should not to be mistaken as a TEV. To determine the presence of TEV, the corresponding pressure coefficient and velocity vector plots should be interpreted together with the vorticity contours. As seen most clearly in Fig. 15(d)(ii), when a TEV is present, the corresponding low pressure zone is created at the trailing edge along with the velocity vector indicating the rotational flow at the trailing edge. As comparison, the corresponding pressure contours do not specify a distinct low pressure zone at the trailing edge, and velocity vectors leave the trailing edge smoothly instead of tracing a rotational flow in Figs. 15(a)–15(c). Therefore, no TEV is present at these instants.

In Fig. 15(d), when C_V is much larger in D8 than that in S8, the main difference is the distinct TEV shown in D8 creating a large low pressure zone on the dorsal surface of the wing, which in turn produces larger upward force as compared to the much smaller low pressure zone in S8. As the wing proceeds further with supination, C_V decreases and reaches a minimum at $\hat{t} = 0.68$ in D8. As seen in Fig. 15(e), the corresponding vorticity and pressure contours in both D8 and S8 are clearly reduced in size and magnitude as compared to those in Fig. 15(d), indicating decreasing vortices strength, thus, the corresponding C_V decreases. Furthermore, at $\hat{t} = 0.68$, the vorticity contours and velocity vectors clearly illustrate that the TEV detaches from the trailing edge in D8, whereas the TEV remains attached at the trailing edge in S8. The pressure contours show that the negative pressure zone shifts to the ventral side of the wing in D8 while the low pressure zone in S8 remains on the dorsal surface, thus explaining the sharp C_V drop in D8. All trends shown in the vortex dynamics in Fig. 15 are in accordance with the time history of force coefficients in Fig. 5.

Referring to the kinematics and vortex dynamics of the wing during supination, we can conclude the following. (1) The large LEV produced at 71% downstroke by delayed stall mechanism does not shed from the wing because as the wing moves further downstroke, the LEV does not continue to gain in size and strength, but gradually reduces its size and strength to maintain its attachment on the dorsal surface of the wing. That is why the LEV inflects at the wing tip to form WTV; the excess vorticity is channelled through the WTV and moves downstream to maintain the stable attachment of the LEV on the wing surface. Furthermore, the WTV forms a counter-rotating vortex comparable with the LEV, which further induces a downward and backward momentum jet in the intervening region of the two counter-rotating vortices pair. (2) The stroke-end rotation occurs in advance of stroke reversal. The nose-down feathering occurs while the wing is still translating forward and downward during supination. Such kinematic motion prevents the wing from interacting with the wake, and provokes the formation of the TEV. The larger downward translational acceleration of the wing in D8 creates a larger TEV on the dorsal surface of the wing, which in turn imparts a larger rate of change of fluid impulse in a very short time period, thus producing the more pronounced vertical force increment than in S8. However, on the downside, the following sharp upward translational acceleration in D8 causes the shedding of TEV and LEV, leaving a negative pressure zone under the wing which produces a sharp drop in the vertical force at 68% of supination. Therefore, in order to utilise the lift enhancing effect of TEV during supination, the kinematics should be arranged such that the wing is accelerating downward and pitching nose-down at the same time. The magnitude of the induced TEV depends on the magnitude of downward acceleration.

VII. CONCLUSIONS

The aerodynamic forces and flow information are presented and compared for the CFD simulations of two different flapping patterns (S8 and D8). The differences between the average lift and drag coefficients in D8 and S8 are marginal. However, the additional lift generating mechanism in D8, which is due to the differences in flapping kinematics, produces larger instantaneous force coefficients during supination and upstroke as compared to S8.

The detailed kinematic and vortex dynamic analyses reveal (1) the mechanism behind LEV stabilization prior to supination, and (2) the kinematic movement responsible for additional lift generation caused by TEV during supination as follows. (1) The LEV produced by delayed stall mechanism during downstroke does not continue to gain in size and strength, but gradually reduces in size and strength, and maintain its attachment on the dorsal surface as the wing proceeds further downstroke. We speculate that the stabilization of the LEV is achieved by channelling exceed vorticity through a WTV. The counter-rotating WTV which moved downstream forms a vortices pair with the LEV. The vortices pair induces a downward and backward momentum jet in the intervening region of the two vortices, which in turn produces an upward and forward force. (2) During supination, the lift enhancing effect of TEV can be manipulated with a simple wing kinematic motion. To achieve large lift increment, the wing kinematics should be arranged such that the wing is accelerating downward and pitching nose-down at the same time.

In our simulations, the wing geometry is kept as a rigid flat plate, and the new lift enhancing mechanism based on this simple geometry boosts lift by changing the kinematic motion of the flapping wing. For easy construction, the design of the geometry and structure of MAVs should be kept as simple as possible. Thus, by changing the kinematic input to enhance lift is much more feasible to implement into flapping MAVs than designing an optimal geometry or structure of the wing itself. By designing the locomotion of the flapping MAVs with the optimised kinematics for lift generation, the performance of the MAVs can be relatively simply improved.

One limitation of our current CFD simulations is neglecting the deformation of the wings during flapping. However, since the computed force and flow information is more sensitive to the geometry of the wings and largely dependent on the flapping patterns integrated, our simulations are unlikely to elicit significant errors on the interpretation and prediction of the results.

Nevertheless, we should not limit our research to rigid wing models. Fluid structure interaction (FSI) simulations reflect the aero-elasticity of the insect wing and the surrounding air. By considering the back-and-forth interaction between the aerodynamics of the flapping wing and the wing deformation caused by the surrounding fluids, the dragonfly wing model can be studied at its most natural state.

ACKNOWLEDGMENTS

Academic Research Fund Tier 1 (Grant No. RG95/13) from the Ministry of Education, Singapore, is greatly acknowledged.

APPENDIX A: PERIODICITY OF FORCE COEFFICIENTS

The wing starts flapping from a stationary position in still air, and the calculation stops when periodicity is approximately reached for the force and flow field generated (in our case is approximately two cycles after the calculation starts, which is in accordance with the simulations done by

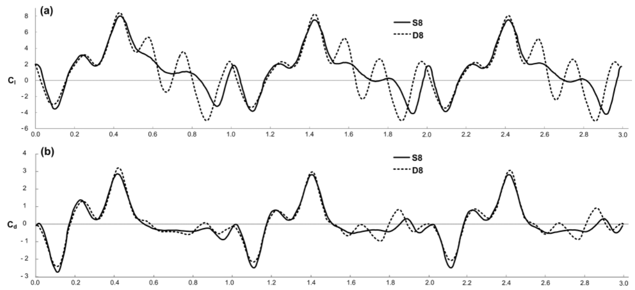

FIG. 16. Computed (a) lift coefficient C_l and (b) drag coefficient C_d in three flapping cycles.

Sun and Lan[28]). In our calculations, three flapping cycles have been simulated; the data from the third cycle are used in our discussions since the periodicity is approximately reached two cycles after the flapping starts. Fig. 16 shows the time course of the force coefficients in these three cycles.

APPENDIX B: KINEMATIC MODELLING

The kinematic model of a typical S8 flapping cycle was expressed in Fourier series as follows:

$$\alpha_s(\hat{t}) = \sum_{n=0}^{6} \left[\alpha_{san} \cos\left(n\hat{t}\right) + \alpha_{sbn} \sin\left(n\hat{t}\right)\right], \tag{B1}$$

$$\phi_{sN}(\hat{t}) = \sum_{n=0}^{6} \left[\phi_{sNan} \cos(n\hat{t}) + \phi_{sNbn} \sin(n\hat{t})\right], \tag{B2}$$

$$\theta_{sN}(\hat{t}) = \sum_{n=0}^{6} \left[\theta_{sNan} \cos(n\hat{t}) + \theta_{sNbn} \sin(n\hat{t})\right]. \tag{B3}$$

Similarly, the kinematic model of a typical D8 flapping cycle was expressed in another set of Fourier series

$$\alpha_d(\hat{t}) = \sum_{n=0}^{6} \left[\alpha_{dan} \cos\left(n\hat{t}\right) + \alpha_{dbn} \sin\left(n\hat{t}\right)\right], \tag{B4}$$

$$\phi_{dN}(\hat{t}) = \sum_{n=0}^{6} \left[\phi_{dNan} \cos(n\hat{t}) + \phi_{dNbn} \sin(n\hat{t})\right], \tag{B5}$$

$$\theta_{dN}(\hat{t}) = \sum_{n=0}^{6} \left[\theta_{dNan} \cos(n\hat{t}) + \theta_{dNbn} \sin(n\hat{t})\right], \tag{B6}$$

where n was an integer from 0 to 6; $\hat{t}$ is the dimensionless time; and the coefficients $\alpha_{san,sbn,dan,dbn}$, $\phi_{sNan,sNbn,dNan,dNbn}$, $\theta_{sNan,sNbn,dNan,dNbn}$ were determined from the measured in-flight kinematic data shown in Fig. 2(c).

[1] A. L. R. Thomas, G. K. Taylor, R. B. Srygley, R. L. Nudds, and R. J. Bomphrey, "Dragonfly flight: Free-flight and tethered flow viualisations reveal a diverse array of unsteady lift-generating mechanisms, controlled primarily via angle of attack," J. Exp. Biol. **207**, 4299-4323 (2004).

[2] C. Somps and M. Luttges, "Dragonfly flight: Novel uses of unsteady separated flows," Science **228**(4705), 1326-1329 (1985).

[3] M. H. Dickinson, F. O. Lehmann, and K. G. Gotz, "The active control of wing rotation by *Drosophila*," J. Exp. Biol. **182**(1), 173-189 (1993).

[4] S. Sunada, L. Zeng, and K. Kawachi, "The relationship between dragonfly wing structure and torsional deformation," J. Theor. Biol. **193**, 39-45 (1998).

[5] C. P. Ellington, "The aerodynamics of hovering insect flight. III. Kinematics," Philos. Trans. R. Soc., B **305**(1122), 41-78 (1984).

[6] S. Sudo, K. Tsuyuki, and J. Tani, "Wing morphology of some insects," JSME Int. J., Ser. C **43**(4), 895-900 (2000).

[7] K. Tsuyuki, S. Sudo, and J. Tani, "Morphology of insect wings and airflow produced by flapping insects," J. Intell. Mater. Syst. Struct. **17**, 743-751 (2006).

[8] J. M. Wakeling and C. P. Ellington, "Dragonfly flight. II. Velocities, accelerations and kinematics of flapping flight," J. Exp. Biol. **200**(3), 557-582 (1997).

[9] W. J. Maybury and F.-O. Lehmann, "The fluid dynamics of flight control by kinematic phase lag variation between two robotic insect wings," J. Exp. Biol. **207**(26), 4707-4726 (2004).

[10] Y. H. Chen, M. Skote, Y. Zhao, and W. M. Huang, "Dragonfly (Sympetrum flaveolum) flight: Kinematic measurement and modelling," J. Fluids Struct. **40**, 115-126 (2013).

[11] H. Wang, L. Zeng, and H. Liu, "Measuring wing kinematics, flight trajectory and body attitude during forward flight and turning maneuvers in dragonflies," J. Exp. Biol. **206**, 745-757 (2003).

[12] Z. J. Wang, "Two dimensional mechanism for insect hovering," Phys. Rev. Lett. **85**(10), 2216 (2000).

[13] T. Weis-Fogh, "Quick estimates of flight fitness in hovering animals, including novel mechanisms for lift production," J. Exp. Biol. **59**, 169-230 (1973).

[14] C. P. Ellington, C. Van den Berg, A. P. Willmott, and A. L. R. Thomas, "Leading-edge vortices in insect flight," Nature **384**(19/26), 626-630 (1996).

[15] C. P. Ellington, "The aerodynamics of hovering insect flight. II. Morphological parameters," Philos. Trans. R. Soc., B **305**(1122), 17-40 (1984).

[16] F. O. Minotti, "Unsteady two-dimensional theory of a flapping wing," Phys. Rev. E **66**(5), 051907 (2002).
[17] S. P. Sane and M. H. Dickinson, "The aerodynamic effects of wing rotation and a revised quasi-steady model of flapping flight," J. Exp. Biol. **205**(8), 1087-1096 (2002).
[18] L. I. Sedov, in *Two-Dimensional Problems in Fuild Dynamics and Aero-Dynamics* (Interscience, New York, 1965), pp. 20-30.
[19] S. Sunada, K. Kawachi, A. Matsumoto, and A. Sakaguchi, "Unsteady forces on a two-dimensional wing in plunging and pitching motions," AIAA J. **39**(7), 1230-1239 (2001).
[20] R. Zbikowski, "On aerodynamic modelling of an insect-like flapping wing in hover for micro air vehicles," Philos. Trans. R. Soc., A **360**(1791), 273-290 (2002).
[21] S. P. Sane, "The aerodynamics of insect flight," J. Exp. Biol. **206**, 4191-4208 (2003).
[22] M. Sun and J. Tang, "Unsteady aerodynamic force generation by a model fruit fly wing in flapping motion," J. Exp. Biol. **205**, 55-70 (2002).
[23] M. H. Dickinson, F.-O. Lehmann, and S. P. Sane, "Wing rotation and the aerodynamic basis of insect flight," Science **284**(5422), 1954-1960 (1999).
[24] Y. H. Chen, M. Skote, Y. Zhao, and W. M. Huang, "Stiffness evaluation of the leading edge of the dragonfly wing via laser vibrometer," Mater. Lett. **97**, 166-168 (2013).
[25] J. K. Wang and M. Sun, "A computational study of the aerodynamics and forewing-hindwing interaction of a model dragonfly in forward flight," J. Exp. Biol. **208**(19), 3785-3804 (2005).
[26] Z. J. Wang, "The role of drag in insect hovering," J. Exp. Biol. **207**(23), 4147-4155 (2004).
[27] S. P. Sane and M. H. Dickinson, "The control of flight force by a flapping wing: Lift and drag production," J. Exp. Biol. **204**(15), 2607-2626 (2001).
[28] M. Sun and S. L. Lan, "A computational study of the aerodynamic forces and power requirements of dragonfly (*Aeschna juncea*) hovering," J. Exp. Biol. **207**(11), 1887-1901 (2004).
[29] H. Liu, C. P. Ellington, K. Kawachi, C. Van Den Berg, and A. P. Willmott, "A computational fluid dynamic study of hawkmoth hovering," J. Exp. Biol. **201**(4), 461-477 (1998).
[30] J. M. Wakeling and C. P. Ellington, "Dragonfly flight. III. Lift and power requirements," J. Exp. Biol. **200**(3), 583-600 (1997).
[31] J. Xu, C. Zhao, Y. Zhang, and Y. Zhang, "Effect of flapping trajectories on the dragonfly aerodynamics," Chin. Sci. Bull. **51**(7), 777-784 (2006).
[32] H. Aono and H. Liu, "Vortical structure and aerodynamics of hawkmoth hovering," J. Biomech. Sci. Eng. **1**(1), 234-245 (2006).
[33] S. N. Fry, R. Sayaman, and M. H. Dickinson, "The aerodynamics of free-flight maneuvers in Drosophila," Science **300**(5618), 495 (2003).
[34] Z. J. Wang, J. M. Birch, and M. H. Dickinson, "Unsteady forces and flows in low Reynolds number hovering flight: Two-dimensional computations vs robotic wing experiments," J. Exp. Biol. **207**, 449-460 (2004).
[35] C. Koehler, T. Wischgoll, D. Haibo, and Z. Gaston, "Vortex visualization in ultra low Reynolds number insect flight," IEEE Trans. Visualization Comput. Graphics **17**(12), 2071-2079 (2011).
[36] H. Nagai, K. Isogai, T. Fujimoto, and T. Hayase, "Experimental and numerical study of forward flight aerodynamics of insect flapping wing," AIAA J. **47**(3), 730-742 (2009).
[37] M. Dickinson, "The effects of wing rotation on unsteady aerodynamic performance at low Reynolds numbers," J. Exp. Biol. **192**(1), 179-206 (1994).
[38] R. B. Srygley and A. L. R. Thomas, "Unconventional lift-generating mechanisms in free-flying butterflies," Nature **420**, 660-664 (2002).
[39] C. P. Ellington, "The aerodynamics of hovering insect flight. IV. Aeorodynamic mechanisms," Philos. Trans. R. Soc., B **305**(1122), 79-113 (1984).
[40] T. Y. Wu, "Fish swimming and bird/insect flight," Annu. Rev. Fluid Mech. **43**(1), 25-58 (2011).
[41] W. B. Dickson and M. H. Dickinson, "The effect of advance ratio on the aerodynamics of revolving wings," J. Exp. Biol. **207**(24), 4269-4281 (2004).
[42] J. M. Birch, W. B. Dickson, and M. H. Dickinson, "Force production and flow structure of the leading edge vortex on flapping wings at high and low Reynolds numbers," J. Exp. Biol. **207**(7), 1063-1072 (2004).
[43] G. Luo and M. Sun, "The effects of corrugation and wing planform on the aerodynamic force production of sweeping model insect wings," Acta Mech. Sin. **21**(6), 531-541 (2005).
[44] M. Okamoto, K. Yasuda, and A. Azuma, "Aerodynamic characteristics of the wings and body of a dragonfly," J. Exp. Biol. **199**, 281-294 (1996).
[45] S. L. Lan and M. Sun, "Aerodynamic properties of a wing performing unsteady rotational motions at low Reynolds number," Acta Mech. **149**(1), 135-147 (2001).
[46] J. M. Birch and M. H. Dickinson, "Spanwise flow and the attachment of the leading-edge vortex on insect wings," Nature **412**, 729-733 (2001).